ARTICLE

Slip Effects on Casson Nanofluid over a Stretching Sheet with Activation Energy: RSM Analysis

Jawad Raza[1], F. Mebarek-Oudina[2,*], Haider Ali[1] and I. E. Sarris[3]

[1]Department of Mathematics, COMSATS University Islamabad, Vehari Campus, Vehari, 61100, Pakistan

[2]Department of Physics, Faculty of Sciences, University of 20 Août 1955-Skikda, Skikda, 21000, Algeria

[3]Department of Mechanical Engineering, University of West Attica, 12244 Athens, Greece

*Corresponding Author: F. Mebarek-Oudina. Email: oudina2003@yahoo.fr; f.mebarek_oudina@univ-skikda.dz

ABSTRACT

The current study is dedicated to presenting the Casson nanofluid over a stretching surface with activation energy. In order to make the problem more realistic, we employed magnetic field and slip effects on fluid flow. The governing partial differential equations (PDEs) were converted to ordinary differential equations (ODEs) by similarity variables and then solved numerically. The MATLAB built-in command 'bvp4c' is utilized to solve the system of ODEs. Central composite factorial design based response surface methodology (RSM) is also employed for optimization. For this, quadratic regression is used for data analysis. The results are concluded by means of tables and pictorial representations. The present study discloses that the temperature profile increases with enhancement in Ha, N_r, N_b, and N_t and it shows opposite behavior for λ. The included parameters show same trend for heat transfer rate (Nu_x). It is also concluded that δ should be maximum for any value of N_b and N_t to maximize the heat transfer rate.

KEYWORDS

Casson nanofluid; activation energy; response surface methodology; optimization

Nomenclature

C	Concentration of nanoparticles ($mol \cdot L^{-1}$)
C_w	The concentration of the wall ($mol \cdot L^{-1}$)
a	Stretching velocity (s^{-1})
T_∞	Free stream temperature (K)
T	Temperature of the nanofluid (K)
T_w	Wall temperature distribution (K)
C_∞	Free nanoparticle concentration ($mol \cdot L^{-1}$)
B_0	Strength of the uniform magnetic field (T)
g	Acceleration due to gravity ($m \cdot s^{-1}$)
D_T	Coefficient of thermophoresis ($m^2 \cdot s^{-1} \cdot K^{-1}$)
D_B	Brownian diffusion coefficient ($m^2 \cdot s^{-1}$)

f	Dimensionless stream function
k	Permeability of porous medium (m^2)
k_1	Ratio of thermal diffusion
c_p	Specific heat at constant pressure $(J \cdot kg^{-1} \cdot K^{-1})$
x, y	Cartesian coordinates along the sheet and normal to it, respectively
u, v	Velocity along x and y axes $(m \cdot s^{-1})$
u_w	Reference velocity $(m \cdot s^{-1})$
θ	Dimensionless temperature
ν	Kinematic viscosity $(m^2 \cdot s^{-1})$
μ	Coefficient of viscosity $(Kg \cdot m^{-1} \cdot s^{-1})$
ρ	The density of the fluid $(Kg \cdot m^{-3})$
σ	Electrical conductivity $(S \cdot m^{-1})$
κ	Thermal conductivity $(W \cdot m^{-1} \cdot K^{-1})$
ϕ	Dimensionless concentration
τ	Ratio of effective heat capacity
η	Similarity variable

1 Introduction

Due to the recent advancements in nanotechnology in the last few decades, the interest of scientists in a special kind of material has developed due to its enhanced thermal transference. Due to the improved thermal efficiency, the nanofluids bring revolution in the fields of thermal engineering and computational fluid dynamics (CFD). The nanoparticles are doping of conventional materials like glycol, ethylene, and mineral oil with extraordinary thermal features. Such kind of suspension of both materials leads to enhanced thermal conductivity and viscosity. It is observed that the surface area of nanoparticles is multiple times greater than that of common fluids. Therefore, the nanoparticles' structure is suggested as microscopic commonly between 1 and 100 nm. Such enhanced thermal materials have many practical applications like chemical processes, mechanical industries, nuclear reactions, cooling processes, solar engineering, extrusion systems, power plants, energy production, etc. Nowadays, nanoparticles are also employed in the medical field like artificial hearts, chemotherapy, cancer tissue damage, X-rays, and surgery processes.

Nanofluids were introduced by Choi et al. [1]. Buongiorno [2] claimed that Brownian and thermophoresis movement is of key importance in the slip transport characteristics. Sheikholeslami et al. [3] considered the different shapes of nanoparticles and selected the best among them in terms of heat transfer. They considered the finite element method (FEM) to compute the findings. The results depicted the increment in the velocity of the nanofluid due to the enhancement in the Darcy and Reynolds number (Re). Ahmad et al. [4] examined Buongiorno's model to examine the impact of thermophoresis and Brownian movement of nanoparticles. They used Von Karman transformations to alter the governing PDEs into ODEs. They observed from the findings that the azimuthal and radial velocities show decreasing and increasing trends with an enhancement in the velocity ratio, respectively. Imtiaz et al. [5] computed the heat transfer rate for single and multi-wall carbon nanotubes (SWCNTs & MWCNTs). The conclusions depicted that the SWCNTs are more effective as compared to MWCNTs in the context of heat transfer rate (Nu_x). Garoosi et al. [6] studied Nu_x for the two-dimensional (2D) nanofluid flow for couples of coolers and heaters. Sheikholeslami et al. [7] analyzed the impact of Brownian motion and thermophoresis parameters for the nanofluid flow among two parallel plates. They employed the differential transformation method to solve the problem and

concluded that the Nusselt number (*Nu*) demonstrates a growing behavior with the increment in Eckert number (*Ec*), Hartmann number (*Ha*), and Schmidt number (*Sc*) and the opposite behavior for the squeeze number (*S*). Mustafa [8] incorporated the Buongiorno model for a rotating disk. They employed the built-in MATLAB collocation routine to solve the problem and the findings depicted that the thermal boundary layer thickness is strengthened due to the existence of thermophoretic force. Turkyilmazoglu [9] analytically analyzed the nanofluid flow through a channel and showed that *Nu* is highly applicable in cooling systems. The study of magnetic dipole influence on a radiative ferromagnetic fluid via a porous stretched sheet was conducted by Dharmaiah et al. [10]. Buongiorno model was employed to study the nanofluid flow over the stretching plate and concluded that the concentration of nanofluid is improved with an enhancement in the melting parameter [11].

There are two basic kinds of nanofluid flow models. i.e., single-phase and two-phase models. Tsuji et al. [12] numerically examined the fluid and motion of particles in a channel and determined empirical parameters related to the collision of particles. Hieu et al. [13] numerically presented the two-phase flow model for simulating wave proliferation in shallow water including wave breaking, reflection, shoaling, and air movement. They demonstrated its capability in simulating wave distortion and breaking. Zeidan et al. [14] described a new solution method for a model of two-phase compressible flows consisting of multiple equations derived from principles of conservation and additional closure governing equations. Ljungqvist et al. [15] used a multi-fluid approach to simulate the problem of two-phase flow in a vessel using CFD code CFX4 and highlighted the importance of slip velocity and particle velocity. Xue et al. [16] proposed a coupling model of groundwater loss and gas drainage to examine the influence of thermally improved methane retrieval on groundwater damage and the ecological risk of coal bed methane growth. Based on the flux equivalent principle, Huang et al. [17] developed a discrete-fractured model of a single fracture, which explicitly describes macroscopic fractures as geometry elements and investigated the effect of fractures on water flooding. Riaz et al. [18] examined the nonlinear development of viscous and gravitational uncertainty in two-phase immiscible movements using numerical methods and described the physical mechanisms of finger progression and interface.

Flow on a stretching surface is extensively recognized by researchers due to its enormous industrial and engineering applications in the manufacturing of food, rubber sheets, hot rolling, glass fiber, paper production, and many others. Activation energy is the minimal energy to be possessed by the particle to endure some kind of change or chemical reaction. The activation energy is mainly applicable in food processing, geothermal engineering, chemical engineering, oil reservoirs, and mechano-chemistry. In various flow conditions like emulsions, polymer solutions, and foam, the slip effects cannot be neglected among the nanofluids and solid boundaries. This phenomenon emerges in numerous applications like nano-channels or micro-channels and in applications where the moving plates are attached to a thin film of light oil or when the surface is sheathed with a unique coating like a thick mono-layer of hydrophobic octadecyl trichlorosilane. Rana et al. [19] examined the laminar boundary layer flow resulting from the nonlinear stretching of a flat surface, taking into account thermophoresis and Brownian motion impacts using the variational FEM. Mabood et al. [20] analyzed the MHD laminar boundary layer flow of nanofluid over a stretching sheet with viscous dissipation and explored the effect of governing parameters on temperature, friction factor, nanoparticle concentration, local *Nu*, and *Sh*. Nadeem et al. [21] numerically examined the two-dimensional boundary layer flow past a stretching sheet, considering the impacts of MHD elasticity, and showed the effect of various parameters on temperature and concentration profiles such as skin friction coefficient (C_{fx}), and Nu_x. Pattnaik et al. [22] examined the impact of chemical reaction on MHD flow through an exponential radiative stretching sheet. They considered the magnetic field and presented its impact on physical

parameters such as velocity, temperature, and concentration profiles. Narayana et al. [23] investigated numerically the influence of the heat source and chemical reaction on MHD Jeffrey fluid flow through stretching sheets with power-law temperature and concentration profiles and examined the effect of various dimensionless parameters on the velocity, temperature, and concentration distributions. Hayat et al. [24] numerically analyzed the boundary-layer flow of a viscous fluid over a stretchable surface, considering the effects of heat absorption/generation and chemical reactions, and investigated the influence of certain parameters on C_{fx}, local Nu and Sh. Mebarek-Oudina et al. [25] established a new Buongiorno model to study magnetized nanofluids flow. Mahanthesh et al. [26] investigated the water-based nanofluid flow caused by a nonlinear stretching surface, incorporating temperature jump boundary condition and transverse magnetic effect, and showed the effects of flow parameters on velocity and temperature distributions, as well as C_{fx} and Nu for different nanoparticles. Ramesh et al. [27] investigated a magnetized Carreau nanofluid with radiation from a flow in a microchannel. Several other works were used to finalize this work [28–30]. Khan et al. [31] explored the heat and mass transfer of ternary hybrid nanomaterials. They concluded that the Darcy-Forchheimer and slip effect were the key parameters in the study. Bejawada et al. [32] studied the MHD micropolar fluid flow and computed the results based on different inclusive parameters. However, the optimization of entropy production with hybrid magneto-nanofluid in porous media are well presented by Mebarek-Oudina et al. [33].

Trusting the literature cited above, we came to know that the problem of Casson nanofluid for activation energy under the influence of magnetic field and slip effects has never been reported before. Therefore, our goal for this problem is to compute the approximate solution of the problem in hand and optimize C_{fx}, heat transfer rate (Nu_x), and Sherwood number (Sh_x) by RSM.

2 Problem Formulation

This portion presents the governing equations for Casson nanofluid based on associated laws. The influence of the magnetic field is observed by considering it vertical to the sheet. Buongiorno's nanofluid model is considered along with thermophoresis and the Brownian impacts. The activation energy is also considered ascribed to the Arrhenius energy. The velocity components are taken as u and v along x and y directions, respectively. Let C be the nanofluid concentration and T be the temperature. The well-known Nield boundary conditions are considered to conduct this study. Furthermore, free stream concentration (C_∞) and the attained free temperature (T_∞) are supposed far away from the sheet [34,35].

$$\frac{\partial u}{\partial x} + \frac{\partial v}{\partial y} = 0 \tag{1}$$

$$u\frac{\partial u}{\partial x} + v\frac{\partial u}{\partial y} = v\left(1 + \frac{1}{\beta}\right)\left(\frac{\partial^2 u}{\partial x^2} + \frac{\partial^2 u}{\partial y^2}\right) - \left(\frac{\sigma^* B_0^2}{\rho_f} + \frac{v\phi}{k^*}\right)u$$

$$+ \left[\frac{(1 - C_\infty)\left(\rho_f \beta^* g\right)(T - T_\infty) - (C - C_\infty)\left(\rho_p - \rho_f\right)g}{\rho_f}\right] \tag{2}$$

$$u\left(\frac{\partial T}{\partial x}\right) + v\left(\frac{\partial T}{\partial y}\right) = \frac{1}{(\rho c_p)_f}\frac{\partial}{\partial y}\left(k\left(T\right)\frac{\partial T}{\partial y}\right) + \frac{Q_0}{(\rho c_p)_f}(T - T_\infty) + \frac{(\rho c_p)_p}{(\rho c_p)_f}\left\{D_B\frac{\partial C}{\partial y}\left(\frac{\partial T}{\partial y}\right) + \frac{D_T}{T_\infty}\left(\frac{\partial T}{\partial y}\right)^2\right\} \tag{3}$$

$$u\left(\frac{\partial C}{\partial x}\right) + v\left(\frac{\partial C}{\partial y}\right) = D_B\left(\frac{\partial^2 C}{\partial y^2}\right) + \frac{D_T}{T_\infty}\left(\frac{\partial^2 T}{\partial y^2}\right) - k_1 r^2 (C - C_\infty)\left(\frac{T}{T_\infty}\right)^2 e^{-Ea/\kappa T} \tag{4}$$

The physical depicters appeared in the above equations are the Casson parameter (β), Stefan-Boltzmann constant (σ^*), magnetic field (B_0), fluid density (ρ_f), permeability of porous medium (k^*), volume suspension coefficient (B^*), gravity (g), nanoparticles density (ρ_p), variable thermal conductivity $\left(k(T) = K_\infty\left(1 + \varepsilon\frac{T-T_\infty}{\Delta T}\right)\right)$, ($Q_0$), diffusion constant ($D_B$), Coefficient of thermophoresis (D_T), activation energy (E_a), the reaction rate ($K_1 r$), and the Boltzmann constant (κ). The term $k_1 r^2 (C - C_\infty)\left(\frac{T}{T_\infty}\right)^2 e^{-Ea/\kappa T}$ in Eq. (4) represents the modified Arrhenius features.

With

$$u = u_w + u_{slip}, v = 0, -k\frac{\partial T}{\partial y} = h_f(T_f - T), D_B\frac{\partial C}{\partial y} + \frac{D_T}{T_\infty}\frac{\partial T}{\partial y} = 0 \text{ at } y = 0 \tag{5}$$

$$u \to 0, \frac{\partial u}{\partial y} \to 0, v \to 0, T \to T_\infty, C \to C_\infty \text{ at } y \to \infty \tag{6}$$

where k, T_f, and h_f represent the thermal conductivity, convective temperature of the fluid, and coefficient of heat transfer, respectively.

The similarity transformations are:

$$\eta = \sqrt{\frac{a}{v}}y, u = cxf'(\eta), v = -avf(\eta), \theta(\eta) = \frac{T - T_\infty}{T_w - T_\infty}, \phi(\eta) = \frac{C - C_\infty}{C_w - C_\infty} \tag{7}$$

The transformed equations and boundary conditions are:

$$\left(1 + \frac{1}{\beta}\right)f''' - (f')^2 + ff'' - Haf' + \lambda(\theta - N_r\phi) = 0 \tag{8}$$

$$(1 + \epsilon\theta)\theta'' + \epsilon\theta'^2 + \Pr\left[N_b\theta'\phi' + f\theta' + N_t\theta'^2 + \delta\theta\right] = 0 \tag{9}$$

$$\phi'' + \frac{N_t}{N_b}\theta'' + LePrf\phi' - LePr\sigma^{**}(1 + \delta\theta)^n \phi e^{(-E/1+\delta\theta)} = 0 \tag{10}$$

With

$$f(0) = 0, f'(0) = 1 + \alpha f''(0), \theta'(0) = Bi(\theta(0) - 1), N_b\theta(0) + N_t\phi'(0) = 0 \tag{11}$$

$$f'(\infty) \to 0, \theta(\infty) \to 0, \phi(\infty) \to 0 \tag{12}$$

where $Ha, \lambda, N_r, \epsilon, Pr, N_b, N_t, Le, \sigma^{**}, Bi$, and E represent the magneto porosity parameter, mixed convective parameter, buoyancy ratio constant, variable thermal conductivity, Prandtl number, Brownian parameter, thermophoresis parameter, Lewis number, reaction constant, Biot number, activation energy, respectively. The values of $Ha, N_r, Pr, N_b, N_t, \delta, Le, Bi$, and E in the mathematical form are [36]:

$$Ha = \frac{\sigma^* B_0^2}{\rho_f c} + \frac{v\phi}{k^* c}, N_r = \frac{(\rho_p - \rho_f)(C_w - C_\infty)}{\beta\rho_f(1 - C_\infty)T_\infty}, Pr = \frac{v}{\alpha_e}, N_b = \frac{(\rho c_p)_p D_B C_\infty}{(\rho c_p)_f v}, N_t = \frac{(\rho c_p)_p D_B(T_f - T_\infty)}{(\rho c_p)_f vT_\infty},$$

$$\delta = \frac{Gc}{v}, Le = \frac{\alpha}{D_B}, Bi = \frac{h_f}{k}\sqrt{\frac{v}{c}}, E = \frac{E_a}{K_1 rT_\infty}$$

The dimensionless form of physical quantities involved in the study are:

$$C_{fx}\sqrt{Re_x} = \left(1 + \frac{1}{\beta}\right)f''(0), \frac{Nu_x}{\sqrt{Re_x}} = -\theta'(0), \frac{Sh_x}{\sqrt{Re_x}} = -\phi'(0)$$

3 Numerical Technique

MATLAB command *'bvp4c'* is utilized to compute the numerical solutions of Eqs. (8)–(10) concerning the boundary conditions (Eqs. (11)–(12)). This is a finite difference scheme that utilizes the Lobatto-III-A formulation. It is a collocation technique with an accuracy of order four. To apply this scheme, the nonlinear ODEs are converted to a system of first-order linear ODEs by introducing the new variables. The residual of the solution is employed to control the error and mesh selection. To employ this function, nonlinear ODEs (Eqs. (8)–(10)) are replaced with the system of first-order ODEs. With the substitutions $y_1 = f, y_2 = f', y_3 = f'', y_4 = \theta, y_5 = \theta', y_6 = \phi, y_7 = \phi'$ and named this system as *'bvp4ode'* in MATLAB. Moreover, the boundary conditions are named *'bvp4bc'*. The interval of integration is taken as 0 to 12 and then discretized into 30 mesh points that construct the initial guess structure. Ultimately, *'bvp4c'* is called with the functions *'bvp4ode'* and *'bvp4bc'* as follows:

$$sol = (@bvp4ode, @bvp4bc, solinit, options)$$

Moreover, to evaluate the solution on specific points, the *'deval'* command is used in MATLAB.

4 Result on Discussions

This portion is devoted to the demonstration of numerical outcomes of the given problem Eqs. (8)–(10) in the form of tables and pictorial structures. The given problem Eqs. (8)–(10) is solved with the help of the three-stage Labotto-III-A formula and the computed values are presented in Table 1.

Table 1: Effect of various parameters on C_{fx}, Nu_x, and Sh_x

Ha	λ	N_r	N_b	N_t	δ	Le	σ^{**}	E	C_{fx}	Nu_x	Sh_x
0.1									−0.89188800		
0.4									−1.00038163		
0.7									−1.09574022		
	0.2								−0.97975676		
	0.5								−0.92362654		
	0.8								−0.87275168		
		0							−0.98938475		
		0.5							−1.04815933		
		1							−1.11067367		
			0.1							0.20572378	
			0.2							0.16836134	
			0.3							0.08292178	
				0.3						0.20198532	
				0.4						0.19710422	
				0.5						0.19182588	
					0.1					0.20572378	

(Continued)

Table 1 (continued)

Ha	λ	N_r	N_b	N_t	δ	Le	σ^{**}	E	C_{fx}	Nu_x	Sh_x
					0.4					0.38929840	
					0.7					0.68954957	
						1					0.57956929
						2					0.57387566
						3					0.57141549
							0.1				0.58855243
							0.3				0.58191833
							0.5				0.57875564
								0.1			0.58855243
								0.2			0.58906797
								0.3			0.58956639

Fig. 1 presents the effect of Ha on the velocity profile ($f'(\eta)$), temperature profile ($\theta(\eta)$), and the concentration profile ($\phi(\eta)$). From this figure, it is depicted that the velocity profile drops as the strength of the magnetic parameter enhances. Physically, it is stated that the boundary layer thickness declines as the magnetic parameter enhances. However, the opposite trend can be seen for the temperature profile. It is because an increase in the magnetic parameter enhances the Brownian effect of the fluid particles which enhances the temperature of the fluid gradually. Therefore, the thermal boundary layer thickness is enhanced as the magnetic parameter increments. A similar trend is seen for the concentration profile.
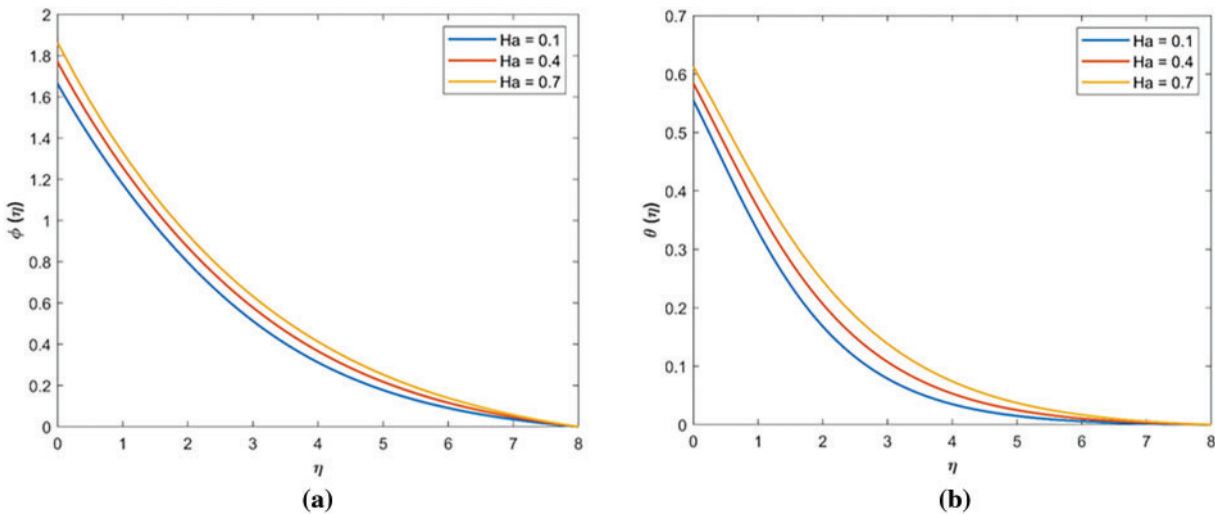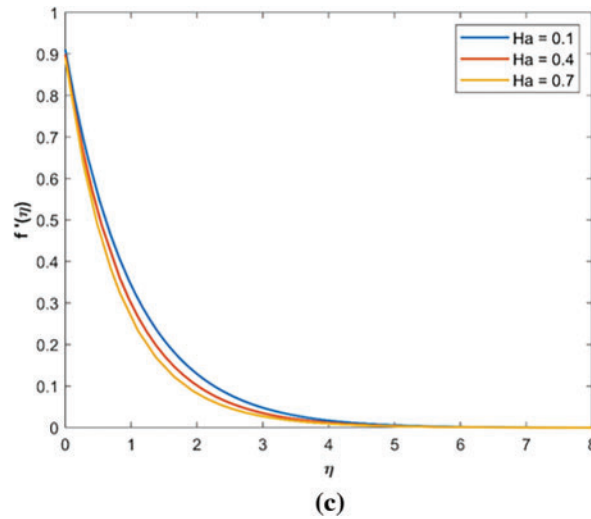

Figure 1: (Continued)

Figure 1: *Ha* effect. (a) Concentration profile against variation of *Ha*. (b) Temperature profile for variations in *Ha*. (c) Velocity profile against variations in *Ha*

The effect of the mixed convective parameter (λ) for the case of assisting flow ($\lambda > 0$) is presented in Fig. 2. From this figure, it came to know that there is a linear relationship between velocity and the values of assisting flow. The boundary layer thickness increases as λ increases. In the case of assisting flow, the buoyancy forces are more prevailing than the viscous forces. Therefore, the boundary layer thickness is enhanced, however contrary behavior is seen for temperature and concentration profiles.
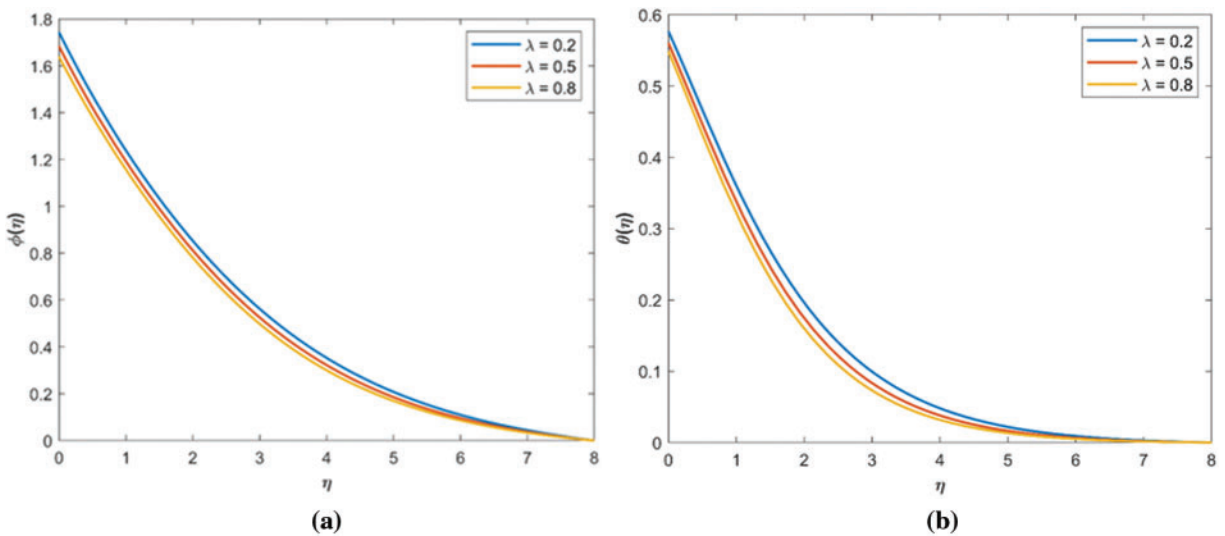
Figure 2: (Continued)

(c)
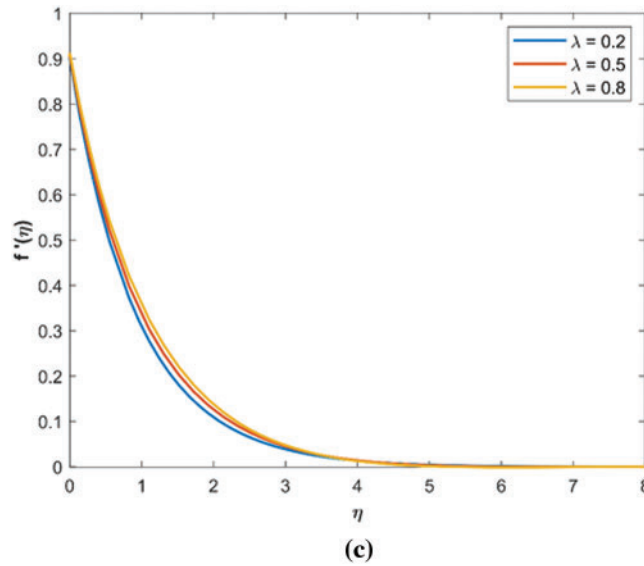
Figure 2: Mixed convective parameter effect (a) Concentration profile for variations in λ. (b) Temperature profile for variations in λ. (c) Velocity profile for variations in λ

The effect of *Nr* is demonstrated in Fig. 3. It can be witnessed that the velocity slows down with an improvement in the values of N_r. It can be seen that the temperature of the nanofluid progresses because of the involvement of the buoyancy ratio forces. The concentration of the nanoparticles in the nanofluid is enhanced due to the enhancement in the buoyancy forces.
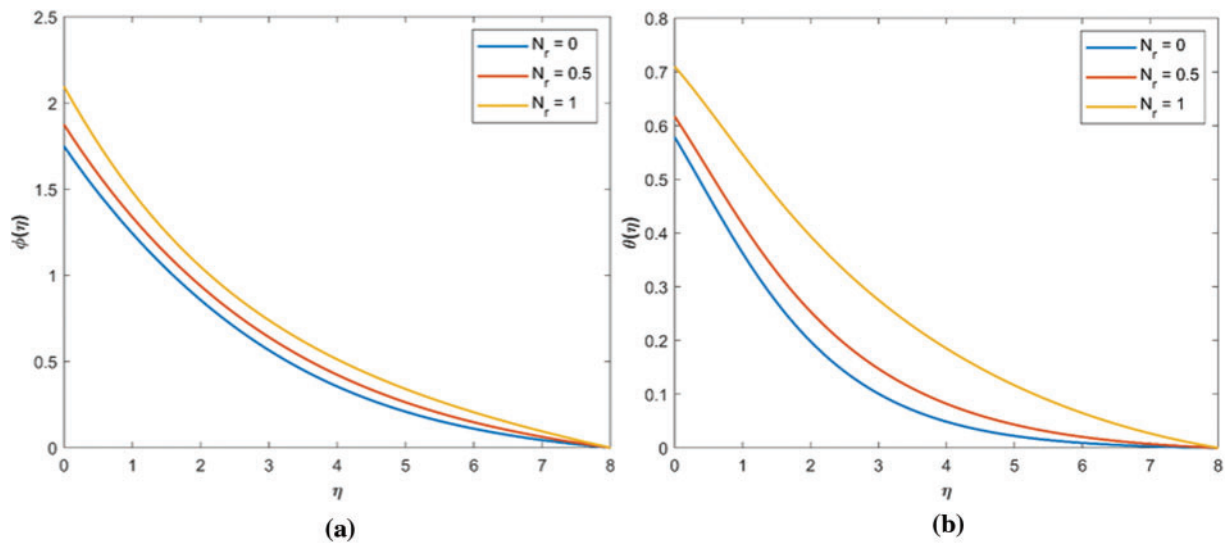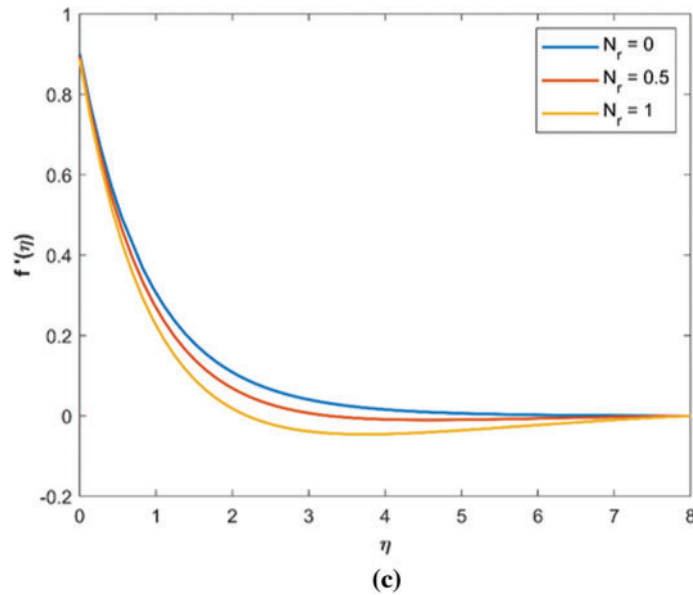

Figure 3: (Continued)

(c)

Figure 3: N_r effect. (a) Concentration profile for variations in N_r. (b) Temperature profile for variations in N_r. (c) Velocity profile for variations in N_r

Fig. 4 presents the impact of N_b on the flow, temperature, and concentration profiles. The Brownian parameter tends to increase the thermal boundary layer thickness when the strength of the Brownian parameter is enhanced. This is because the increment in the Brownian parameter allows the particles to migrate from one place to another. So, this is the reason why the collateral resistance between the fluid particles enhances the temperature of the fluid. Therefore, the concentration and the thermal boundary layer thickness increase rapidly. A similar effect on temperature and concentration is seen in the case of N_t as presented in Fig. 5.
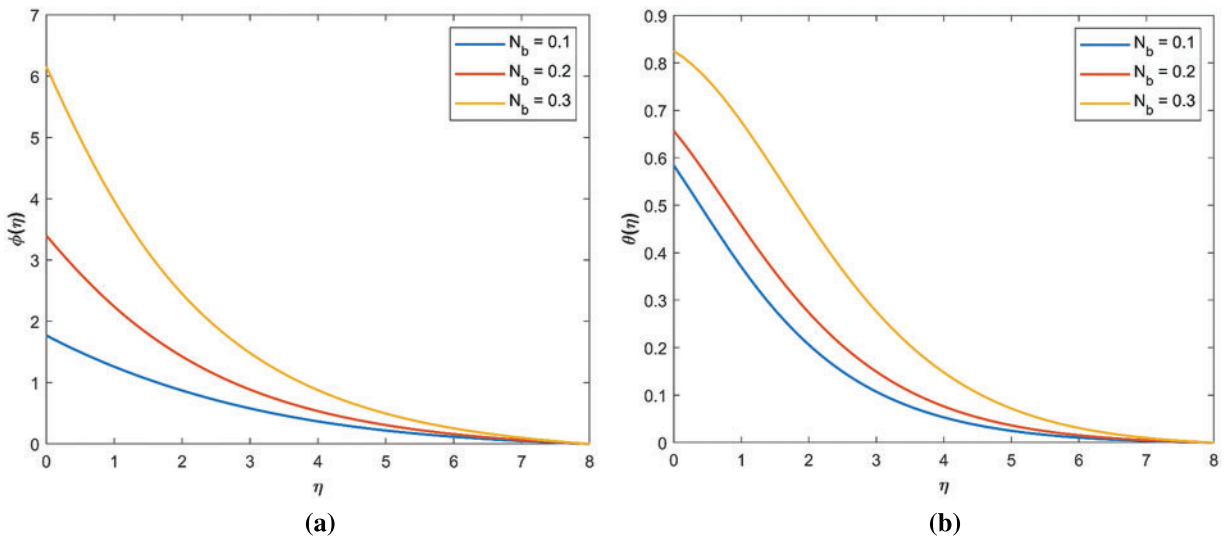

(a)

(b)

Figure 4: N_b effect. (a) Effect of N_b on concentration profile. (b) Effect of N_b on the temperature profile
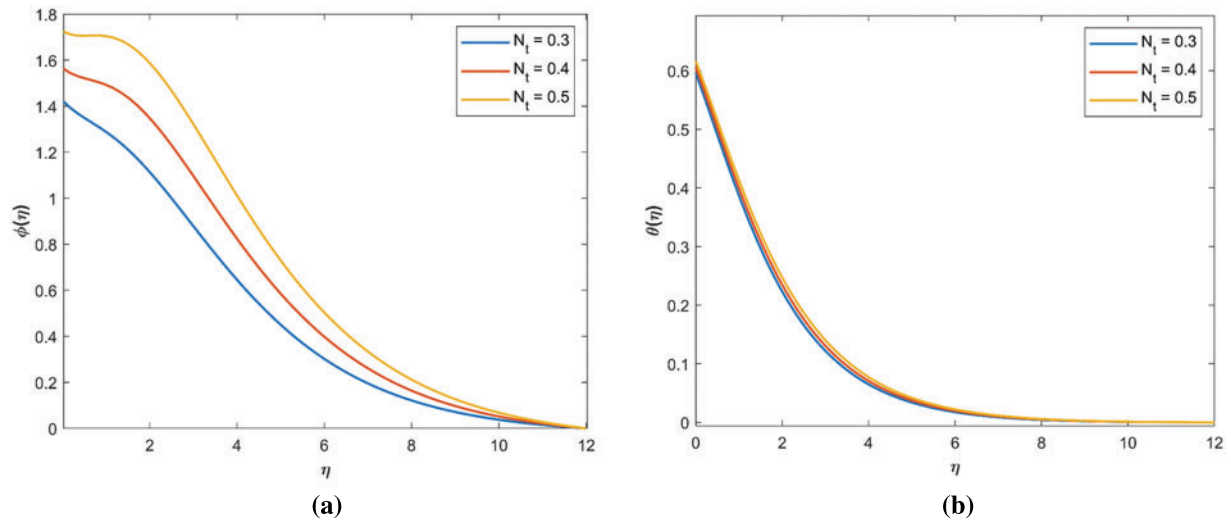
Figure 5: N_t effect. (a) Impact of N_t on concentration profile. (b) Impact of N_t on the temperature profile

Fig. 6 is plotted to observe the impact of *Le* on the concentration of nanoparticles. It is seen that the concentration distribution curve decreases with an enhancement in *Le*. Due to the enhancement in *Le*, the mass diffusivity becomes smaller which results in the reduction of $\phi(\eta)$. The impact of σ^{**} on the concentration profile is presented in Fig. 7. The concentration process slows down due to the presence of σ^{**}. The chemical reaction becomes more effective due to the existence of activation energy. The concentration of nanoparticles is enhanced due to the enhancement in *E* as presented in Fig. 8.
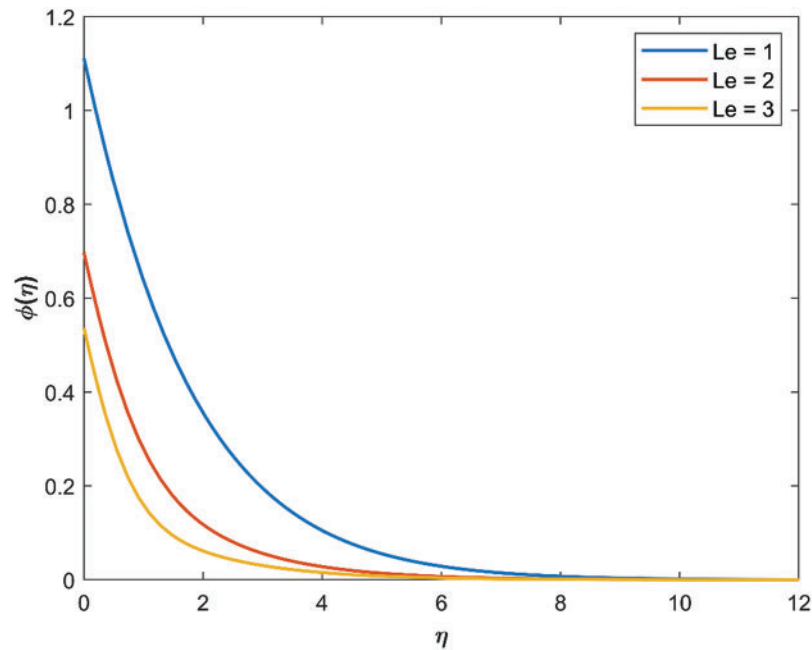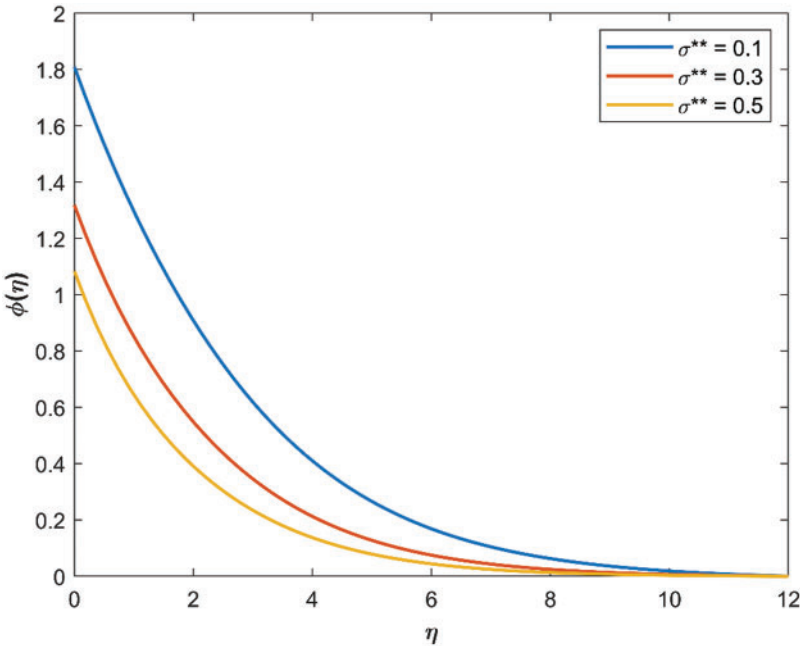

Figure 6: Effect of *Le* on concentration profile

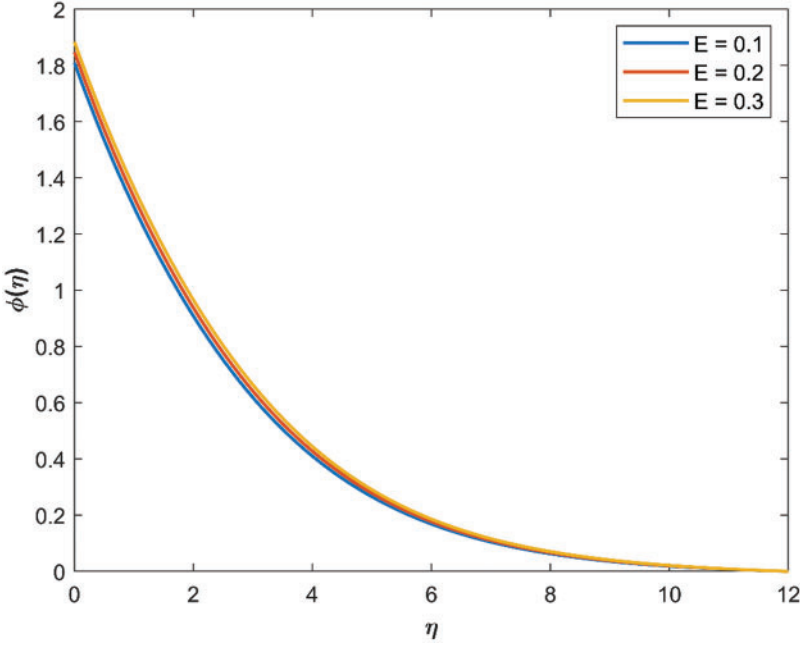**Figure 7:** Effect of σ^{**} on concentration profile

Figure 8: Effect of E on concentration profile

4.1 Optimization Process

RSM is a powerful tool to describe a broad range of variables, with partial resources, quantitative data, and the mandatory test design. The stages involved in RSM are as follows:

1. The investigation of data values is planned and executed to achieve appropriate and credible requirements for the projected response.
2. The most suitable mathematical models were described for the response surface.
3. It was defined that the mathematical models of the response surface are the most suitable.
4. To inspect the parametric direct and interaction impacts (ANOVA), variance analysis was done.

4.2 Optimization Analysis by RSM

The relation among the response variable and factor variables was computed by employing a face-centered central composite design. Tables 2–4 describe the inclusive factors and levels. The model is described in (13), in which the linear, square, and interactive terms are involved.

Table 2: Parameters with their levels for C_{fx}

Parameters	Symbols	Level		
		−1	0	1
Ha	A	0.1	0.4	0.7
λ	B	0.2	0.5	0.8
N_r	C	0	0.5	1

Table 3: Parameters with their levels for Nu_x

Parameters	Symbols	Level		
		−1	0	1
N_b	A	0.1	0.2	0.3
N_t	B	0.3	0.4	0.5
δ	C	0.1	0.4	0.7

Table 4: Parameters with their levels for Sh_x

Parameters	Symbols	Level		
		−1	0	1
Le	A	1	2	3
σ^{**}	B	0.1	0.3	0.5
E	C	0.1	0.2	0.3

Response =

$$\alpha_0 + \alpha_1 A + \alpha_2 B + \alpha_3 C + \alpha_{11} A^2 + \alpha_{22} B^2 + \alpha_{33} C^2 + \alpha_{12} AB + \alpha_{13} AC + \alpha_{23} BC \qquad (13)$$

4.2.1 Response Surface Regression: $C_{fx}(0)$ vs. Ha, λ and N_r

This section examined the response of three factors Ha, λ, and N_r. The optimum mode is defined and the sensitivity analysis of influential factors on $C_{fx}(0)$ is performed. Table 5 represents the values of the response function for 20 different points.

Table 5: Experimental design and responses

Runs	Coded values			Responses		
	A	B	C	C_{fx}	Nu_x	Sh_x
1	0	0	0	−0.39684751	0.40782807	0.11948642
2	1	−1	−1	−0.57886420	0.19265987	0.11966147.
3	0	1	0	−0.29209551	0.40365355	0.11921239
4	0	0	0	−0.39684751	0.40782807	0.11948642
5	−1	−1	−1	−0.46387103	0.20867705	0.12113372
6	0	0	−1	−0.38716713	0.20091253	0.11943170
7	1	1	1	−0.27978532	0.68712455	0.11908986
8	0	0	0	−0.39684751	0.40782807	0.11948642
9	−1	−1	1	−0.42894289	0.67801826	0.12130162
10	1	−1	1	−0.58417418	0.69846539	0.11972700
11	0	0	0	−0.39684751	0.40782807	0.11948642
12	1	1	−1	−0.34240632	0.19195249	0.11902415
13	0	0	0	−0.39684751	0.40782807	0.11948642
14	0	0	0	−0.39684751	0.40782807	0.11948642
15	−1	0	0	−0.45421693	0.40410961	0.12014734
16	0	−1	0	−0.56036217	0.41146684	0.12009442
17	0	0	1	−0.34204689	0.68475116	0.11954209
18	1	0	0	−0.48377248	0.40703194	0.11925364
19	−1	1	1	−0.06080642	0.65995862	0.11975680
20	−1	1	−1	−0.23690397	0.20101396	0.11959444

i) Statistical Analysis

Based on the given settings. The statistical analysis executed 20 runs for $C_{fx}(0)$,. The Tables 6 and 7 show the coded coefficient and statistical analysis influence. This model is appropriate for calculating the value of $C_{fx}(0)$ because a better value of R^2 for $C_{fx}(0)$, i.e., 96.25% was attained by the statistical scheme and statistical study of the model. Further, the R^2-Adj amount for $C_{fx}(0)$ is 92.88% is less than R^2 but the model fits experimental data acceptably.

Table 6: Coded coefficients

Term	Coef	SE Coef	T-value	p-value	VIF
Constant	−0.4105	0.0111	−36.84	0	
Ha	−0.0624	0.0103	−6.09	0	1.00
λ	0.1404	0.0103	13.70	0.000	1.00
N_r	0.0313	0.0103	3.06	0.012	1.00
$Ha * Ha$	−0.0379	0.0195	−1.94	0.081	1.82
$\lambda * \lambda$	0.0049	0.0195	0.25	0.809	1.82
$N_r * N_r$	0.0665	0.0195	3.40	0.007	1.82
$Ha * \lambda$	−0.0068	0.0115	−0.59	0.567	1.00
$Ha * N_r$	−0.0192	0.0115	−1.68	0.125	1.00
$\lambda * N_r$	0.0261	0.0115	2.28	0.046	1.00

Table 7: Analysis of variance

Source	DF	Adj SS	Adj MS	F-value	p-value
Model	9	0.269880	0.029987	28.54	0
Linear	3	0.245978	0.081993	78.03	0
Ha	1	0.038970	0.038970	37.09	0
λ	1	0.197183	0.197183	187.66	0
N_r	1	0.009826	0.009826	9.35	0.012
Square	3	0.015115	0.005038	4.80	0.025
$Ha * Ha$	1	0.003951	0.003951	3.76	0.081
$\lambda * \lambda$	1	0.000065	0.000065	0.06	0.809
$N_r * N_r$	1	0.012155	0.012155	11.57	0.007
2-way interaction	3	0.008787	0.002929	2.79	0.096
$Ha * \lambda$	1	0.000368	0.000368	0.35	0.567
$Ha * N_r$	1	0.002954	0.002954	2.81	0.125
$\lambda * N_r$	1	0.005465	0.005465	5.20	0.046
Error	10	0.010508	0.001051		
Lack-of-fit	5	0.010508	0.002102	*	*
Pure error	5	0	0		
Total	19	0.280388			

ii) Analysis of Variance and Model Estimation:

To achieve the projected regression equation, experimental model presented in Table 8 is executed under altered experimental settings. The residual plot is achieved by analysis of variance and entering the data into analytical software.

Table 8: Model summary

S	R-sq	R-sq (adj)	R-sq (pred)
0.0324154	96.25%	92.88%	72.13%

From Table 7, it is noticed that p-value of $Ha^2, \lambda^2, Ha*\lambda, Ha*N_r > 0.05$. Therefore Ha^2, λ^2, $Ha*\lambda, Ha*N_r$ has an insignificant impact on the Response function $C_{fx}(0)$.

iii) Regression Equation in Uncoded Units

$$C_{fx}(0) = -0.5772 + 0.231Ha + 0.357\lambda - 0.2391N_r - 0.421Ha^2 + 0.054\lambda^2 + 0.2659N_r^2$$
$$- 0.075Ha*\lambda - 0.1281Ha*N_r + 0.1743\lambda*N_r \tag{14}$$

From Table 8 it is noticed that the p-value of $Ha^2, \lambda^2, Ha*\lambda, Ha*N_r > 0.05$. Therefore Ha^2, λ^2, $Ha*\lambda, Ha*N_r$ has an insignificant impact on the Response function $C_{fx}(0)$.

After removing the factors which have a p-value greater than 0.05 the regression equation for $C_{fx}(0)$ is reduced to the following equation:

$$C_{fx}(0) = -0.5772 + 0.231Ha + 0.357\lambda - 0.2391N_r + 0.2659N_r^2 + 0.1743\lambda*N_r \tag{15}$$

iv) Residual and Surface Plots

The residual plot is given in Fig. 9a. In the residual plot difference in observed y-value (from the scattered plot) and predicted y-value is known as residual. According to the figure normal probability plot is in good condition because all the points near the approximate straight lines which represent normality. In residual Histogram halves do not appear as a mirror image so is skew symmetrical distribution. Observed and fitted values display a good correlation if compared to the residual diagram and fitted value. The greatest residual was observed to be in the proximity of 0.025 for $C_{fx}(0)$. By applying RSM we get Eq. (1) which is a common relationship between their effective factors.

Fig. 9b represents $C_{fx}(0)$ with N_r and λ as variables. Here we observed changes in Reynolds number and wavelength affect the coefficient of friction at the leading edge. Higher Reynolds numbers tend to increase $C_{fx}(0)$ due to increased turbulence and thicker boundary layers, while the impact of wavelength depends on the relative size compared to relevant length scales in the flow.

Fig. 9c observed the influence of λ and Ha on $C_{fx}(0)$. The impact of λ on $C_{fx}(0)$ depends on the relative size of the wavelength compared to the characteristic length scales of the flow. If the wavelength is small compared to the boundary layer thickness or other relevant length scales, its effect on $C_{fx}(0)$ may be minimal. However, if the wavelength is comparable to or larger than these length scales, it can significantly influence the flow behavior and, consequently, $C_{fx}(0)$. The influence of Ha on $C_{fx}(0)$ is related to the suppression of flow turbulence by the magnetic field. A higher Hartmann number (stronger magnetic field) tends to suppress turbulence and stabilize the flow, resulting in a smoother flow near the leading edge. As a result, $C_{fx}(0)$ may decrease under the influence of a higher Ha, indicating reduced friction at the leading edge. The three-dimensional surface plot in Fig. 9d presents the impact of N_r and Ha on the response function. The maximum value of the response function occurs when we increase the value of N_r and Ha.
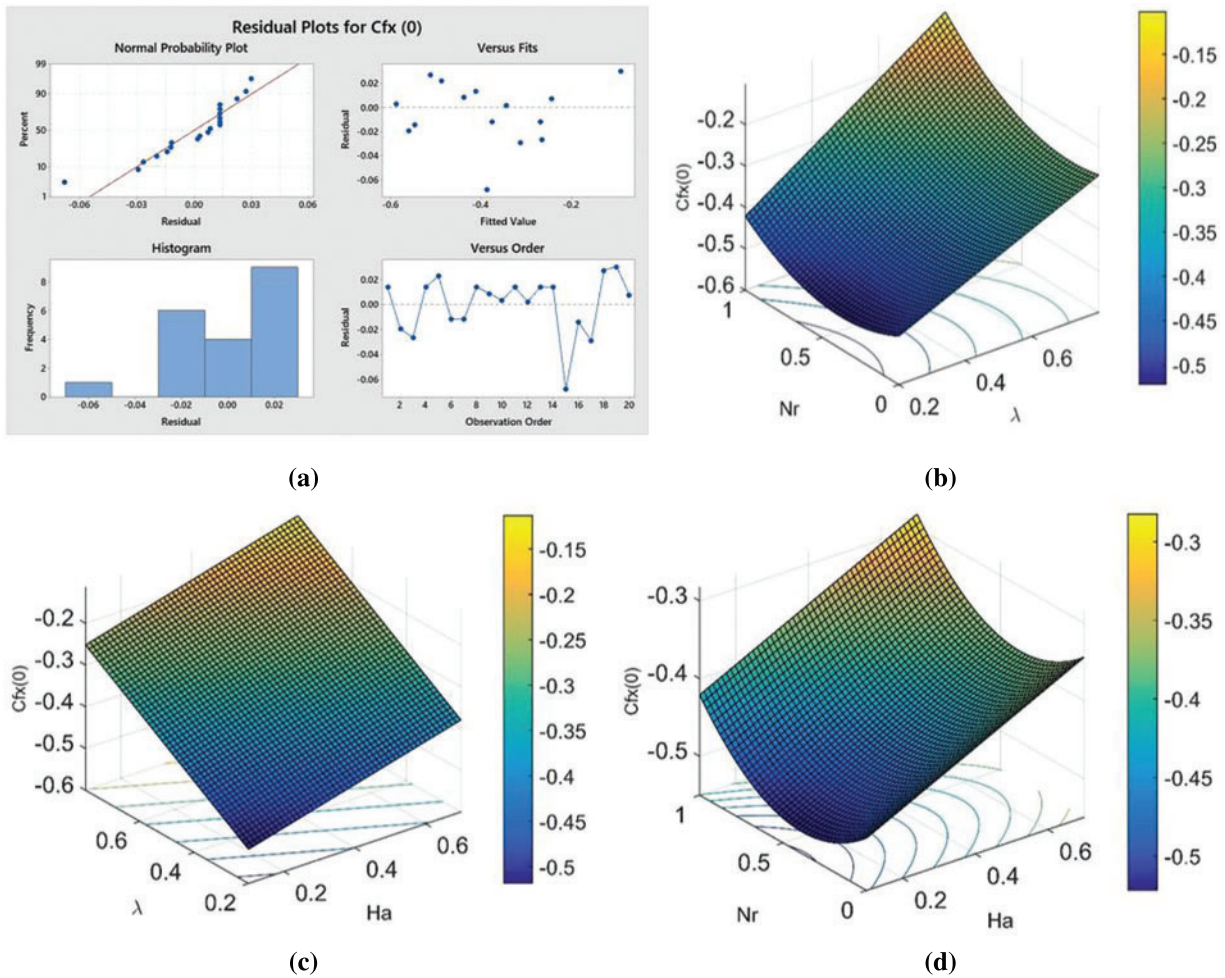
Figure 9: Influential factors on $C_{fx}(0)$. (a) Residual plot. (b) Influence of N_r and λ on $C_{fx}(0)$. (c) Influence of λ and Ha on $C_{fx}(0)$. (d) Impact of N_r and Ha on response function

4.2.2 Response Surface Regression: $Nu_x(0)$ vs. N_b, N_t, δ

In this section, the response of three factors N_b, N_t, δ on $Nu_x(0)$ is examined. The optimum mode is defined and the sensitivity analysis of influential factors on to perform $Nu_x(0)$ is executed

i) Statistical Analysis:

According to the given settings, the statistical analysis executed 20 runs for $Nu_x(0)$. Tables 9 and 10 show the coded coefficient and statistical analysis effect. This model is appropriate for calculating the value of $Nu_x(0)$ because a better value of R^2 for Nu_x, i.e., 100% which is attained by statistical scheme and statistical analysis of the model. Further, the $R^2 - Adj$ amount for Nu_x is 100%. 100% of R^2 represents a model that enlightens all the variation in the response variable around its mean. Generally, the greater the R^2, The improved regression model fits our observations.

Table 9: Coded coefficients

Term	Coef	SE Coef	T-value	p-value	VIF
Constant	0.407911	0.000245	1664.75	0	
N_b	0.002546	0.000225	11.29	0	1.00
N_t	−0.004558	0.000225	−20.22	0	1.00
σ^{**}	0.241310	0.000225	1070.62	0	1.00
$N_b * N_b$	−0.002466	0.000430	−5.74	0	1.82
$N_t * N_t$	−0.000476	0.000430	−1.11	0.294	1.82
$\sigma^{**} * \sigma^{**}$	0.034795	0.000430	80.96	0	1.82
$N_b * N_t$	0.001709	0.000252	6.78	0	1.00
$N_b * \sigma^{**}$	0.009086	0.000252	36.06	0	1.00
$N_t * \sigma^{**}$	−0.002629	0.000252	−10.43	0	1.00

Table 10: Analysis of variance

Source	DF	Adj SS	Adj MS	F-value	p-value
Model	9	0.588796	0.065422	128777.83	0
Linear	3	0.582579	0.194193	382254.13	0
N_b	1	0.000065	0.000065	127.56	0
N_t	1	0.000208	0.000208	409.02	0
σ^{**}	1	0.582306	0.582306	1146225.79	0
Square	3	0.005478	0.001826	3594.36	0
$N_b * N_b$	1	0.000017	0.000017	32.91	0
$N_t * N_t$	1	0.000001	0.000001	1.23	0.294
$\sigma^{**} * \sigma^{**}$	1	0.003329	0.003329	6553.85	0
2-way interaction	3	0.000739	0.000246	485.00	0
$N_b * N_t$	1	0.000023	0.000023	46.01	0
$N_b * \sigma^{**}$	1	0.000661	0.000661	1300.17	0
$N_t * \sigma^{**}$	1	0.000055	0.000055	108.82	0
Error	10	0.000005	0.000001		
Lack-of-fit	5	0.000005	0.000001	*	*
Pure error	5	0	0		
Total	19	0.588801			

ii) Analysis of Variance and Model Estimation:

To get the approximate regression equation, the experimental model presented in Table 11 is executed under changed experimental settings. The residual plot is achieved by analysis of variance and entering the data into analytical software. By applying RSM we get Eq. (16) which is a frequent relationship between their valuable factors.

Table 11: Model summary

S	R-sq	R-sq (adj)	R-sq (pred)
0.0007128	100.00%	100.00%	99.99%

From Table 10, it is observed that the p-value of $N_t^2 > 0.05$. Therefore N_t^2 has an inconsequential influence on Response function Nu_x.

iii) Regression Equation in Uncoded Units

$$Nu_x(0) = 0.16757 - 0.0654N_b - 0.0066N_t + 0.46955\sigma^{**} - 0.2466N_b * N_b - 0.0476N_t * N_t$$

$$+ 0.38662\sigma^{**} * \sigma^{**} + 0.1709N_b * N_t + 0.30288N_b * \sigma^{**} - 0.08763N_t * \sigma^{**} \quad (16)$$

From Table 11, it is observed that the p-value of $N_t^2 > 0.05$ therefore N_t^2 has an inconsequential influence on Response function Nu_x.

After eliminating the factors which have a p-value greater than 0.05 the regression equation for $Nu_x(0)$ is reduced to the below equation

$$Nu_x(0) = 0.16757 - 0.0654N_b - 0.0066N_t + 0.46955\sigma^{**} - 0.2466N_b * N_b + 0.38662\sigma^{**} * \sigma^{**}$$

$$+ 0.1709N_b * N_t + 0.30288N_b * \sigma^{**} - 0.08763N_t * \sigma^{**} \quad (17)$$

iv) Residual and Surface Plots

The residual plot is given in Fig. 10a. In the residual plot difference observed from the scattered plot and predicted y-value is known as residual. According to the figure normal probability plot is in good condition because all the points near the approximate straight lines which represent normality. In residual Histogram halves do not appear as a mirror image so it skews symmetrical distribution. Observed and fitted values display a good correlation if compared to the residual diagram and fitted value. The maximum residual was observed to be in the proximity of 0.0015 for $Nu_x(0)$. In Fig. 10b displayed the effect of N_b and N_t on response function. The response function showed the largest value when N_b decreased and for any value of N_t. The impact of δ and N_b is displayed in the Fig. 10c. The high value of the response function is observed at the high values of δ and N_b. The interaction of δ and N_t is showen in Fig. 10d. The maximum value of $Nu_x(0)$ occurs for increased value of δ and any value of N_t.

4.2.3 Response Surface Regression: $Sh_x(0)$ vs. Le, σ^{**}, E

In this section, the response of three factors of Le, σ^{**}, E on $Sh_x(0)$. The optimum mode is described and the sensitivity analysis of influential factors on $Sh_x(0)$ is performed.

i) Statistical Analysis:

According to specified settings. The statistical analysis executed 20 runs for $Sh_x(0)$. Tables 12 and 13 demonstrate the coded coefficient and statistical analysis influence. This model is appropriate for determining the value of Nu_x because the better value of R^2 for $Sh_x(0)$. i.e., 99.54% which was attained by the statistical scheme and statistical analysis of the model. Further, the $R^2 - Adj$ amount for $Sh_x(0)$ is 99.12%, which is lower than R^2, but the model fits experimental data suitably.
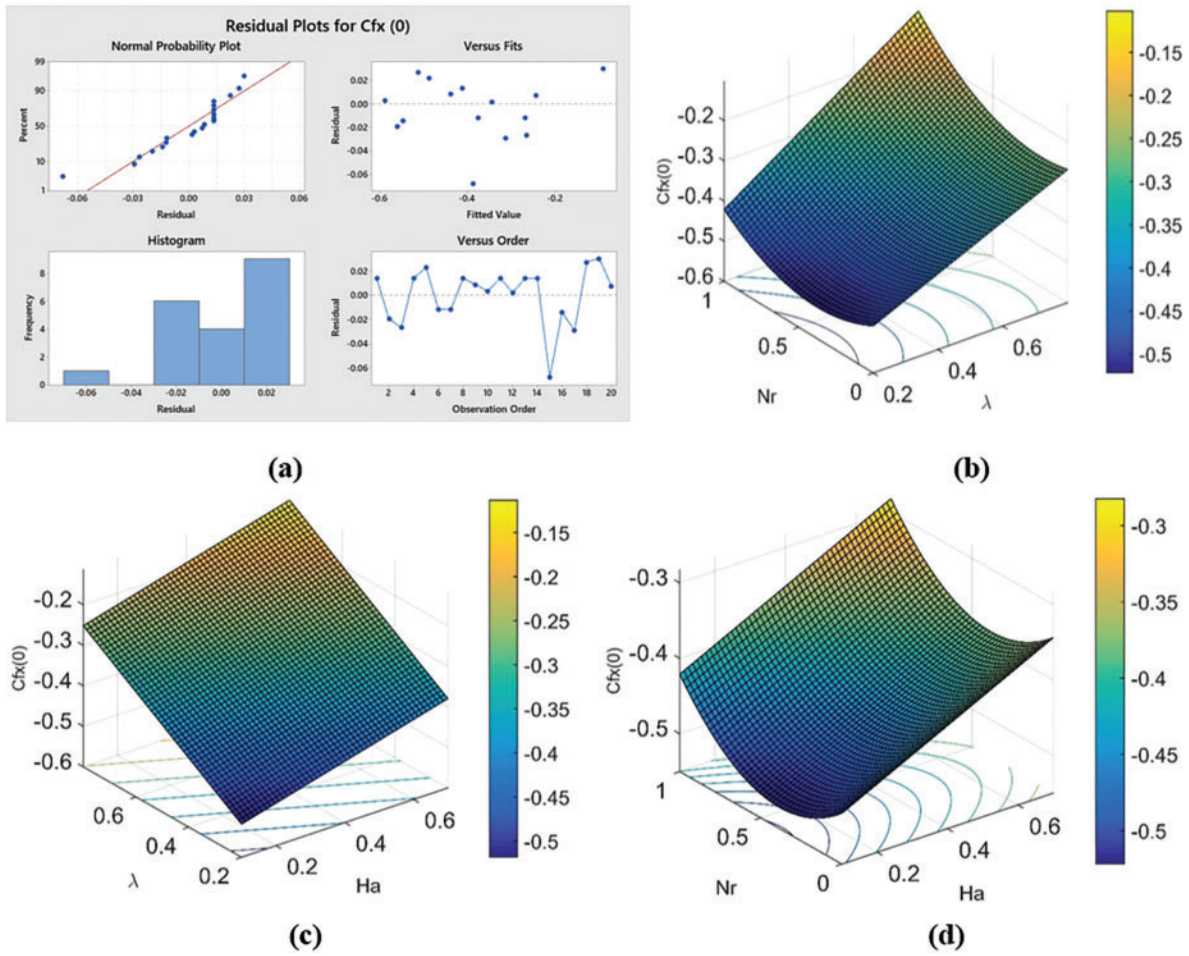
Figure 10: Influential factors on $Nu_x(0)$ (a) Residual plot. (b) Effect of N_b and N_t on $Nu_x(0)$. (c) Impact of δ and N_b on $Nu_x(0)$. (d) Interaction of δ and N_t on $Nu_x(0)$

Table 12: Coded coefficients

Term	Coef	SE Coef	T-value	*p*-value	VIF
Constant	0.119480	0.000019	6278.16	0	
Le	−0.000518	0.000018	−29.58	0	1.00
σ^{**}	−0.000524	0.000018	−29.94	0	1.00
E	0.000057	0.000018	3.27	0.008	1.00
$Le * Le$	0.000230	0.000033	6.88	0	1.82
$\sigma^{**}\sigma^{**}$	0.000183	0.000033	5.47	0	1.82
$E * E$	0.000016	0.000033	0.48	0.638	1.82
$Le * \sigma^{**}$	0.000226	0.000020	11.56	0	1.00
$Le * E$	−0.000025	0.000020	−1.27	0.232	1.00
$\sigma^{**} * E$	−0.000001	0.000020	−0.03	0.973	1.00

Table 13: Analysis of variance

Source	DF	Adj SS	Adj MS	F-value	p-value
Model	9	0.000007	0.000001	239.23	0
Linear	3	0.000005	0.000002	593.88	0
Le	1	0.000003	0.000003	874.81	0
σ^{**}	1	0.000003	0.000003	896.16	0
E	1	0	0	10.67	0.008
Square	3	0.000001	0	78.75	0
$Le * Le$	1	0	0	47.38	0
$\sigma^{**} * \sigma^{**}$	1	0	0	29.95	0
$E * E$	1	0	0	0.23	0.638
2-Way Interaction	3	0	0	45.06	0
$Le * \sigma^{**}$	1	0	0	133.57	0
$Le * E$	1	0	0	1.62	0.232
$\sigma^{**} * E$	1	0	0	0	0.973
Error	10	0	0		
Lack-of-Fit	5	0	0	*	*
Pure Error	5	0	0		
Total	19	0.000007			

ii) Analysis of Variance and Model Estimation:

To get the approximate regression equation of the experimental model presented in Table 14 is executed under transformed experimental settings. The residual plot is achieved by analysis of variance and entering the data into analytical software. By using RSM we get Eq. (18) which is a numerous relationship between their helpful factors.

Table 14: Model summary

S	R-sq	R-sq (adj)	R-sq (pred)
0.0000554	99.54%	99.12%	96.45%

From Table 13 it is observed that the p-value of $E^2, Le * E, \sigma^{**} * E > 0.05$ therefore $E^2, Le * E, \sigma^{**} * E$ has negligible influence on Response function $Sh_x(0)$.

iii) Regression Equation in Uncoded Units

$$Sh_x(0) = 0.123159 - 0.001726Le - 0.007616\sigma^{**} + 0.00043E + 0.000230Le * Le$$
$$+ 0.004567\sigma^{**} * \sigma^{**} + 0.00162E * E + 0.001131Le * \sigma^{**} - 0.000249Le * E$$
$$- 0.000033\sigma^{**} * E \tag{18}$$

From Table 14 it is observed that the p-value of $E^2, Le * E, \sigma^{**} * E > 0.05$ therefore $E^2, Le * E, \sigma^{**} * E$ has negligible influence on Response function $Sh_x(0)$.

After eliminating the factors which have a *p*-value greater than 0.05 the regression equation for $Sh_x(0)$ is reduced to the below equation:

$$Sh_x(0) = 0.123159 - 0.001726Le - 0.007616\sigma^{**} + 0.00043E + 0.000230Le*Le$$
$$+ 0.004567\sigma^{**}*\sigma^{**} + 0.001131Le*\sigma^{**} \tag{19}$$

iv) Residual and Surface Plots

The residual plot is given in Fig. 11a. In the residual plot difference observed from the scattered plot and predicted *y*-value is known as residual. According to the figure normal probability plot is in good condition because all the points near the approximate straight lines which represent normality. In the residual histogram, halves do not appear as a mirror image so there is skew symmetrical distribution. Observed and fitted values display a good correlation if compared to the residual diagram and fitted value. The maximum residual was observed to be in the proximity of 0.00008 for $Sh_x(0)$. Fig. 11b illustrates the consequence of σ^{**} and *Le* on response function, the response function attained maximum value for the minimal value of σ^{**} and *Le*. Fig. 11c,d elucidated the impact of E^{**}, *Le* and on response function. The highest value of the response function is observed at low value of Le, σ^{**} and all values of E^{**}.
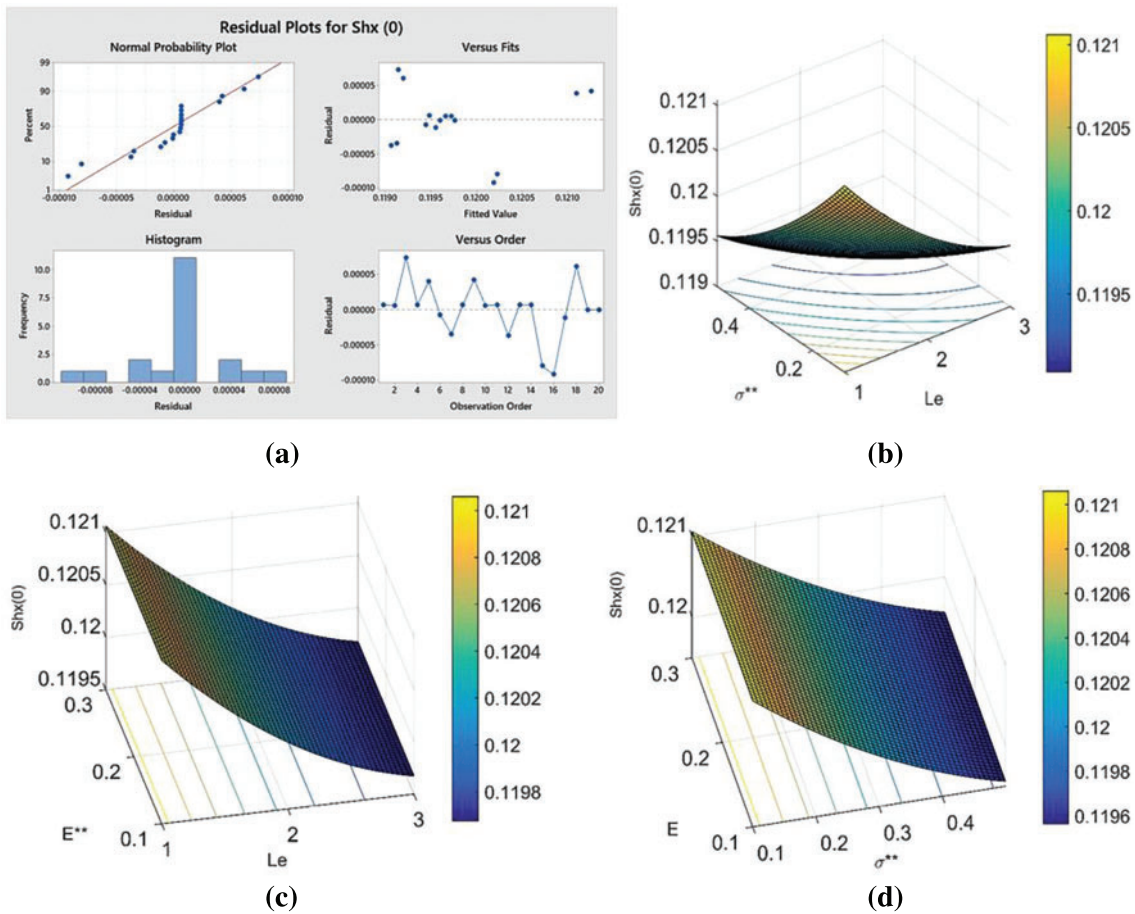

Figure 11: Influential factors on $Sh_x(0)$ (a) Residual plot. (b) Consequence of σ^{**} and *Le* on $Sh_x(0)$. (c) Impact of E^{**} and *Le* on $Sh_x(0)$. (d) Impact of E^{**} and σ^{**} on $Sh_x(0)$

5 Conclusion

In this study, the Casson nanofluid was examined, and its thermal analysis and optimizations were conducted. The following conclusions can be drawn:

- The velocity profile decreases with an increment in Ha and N_r, exhibiting the opposite trend for an increase in λ. The comprehensive parameters demonstrate a similar trend for C_{fx}.
- The temperature profile rises with enhancement in Ha, N_r, N_b, and N_t, showing the opposite behavior for λ. The incorporated parameters reveal a consistent pattern for the heat transfer rate (Nu_x).
- The concentration profile increases with rising values of Ha, N_r, N_b, N_t, and E while displaying an opposing trend for λ, Le, and σ^{**}. The inclusive parameters show the same trend for Sh_x.
- Nu_x maximizes for $N_b = 0.1$ and $N_t = 0.5$.
- For higher values of δ, Nu_x is maximum when $N_b = [0.1, 0.3]$, $N_t = [0.3, 0.5]$. So, δ should be the maximum for any value of N_b and N_t to maximize the heat transfer rate.
- This work can be extended to hybrid and ternary hybrid nanofluids. Furthermore, the application of artificial neural networks could further optimize the study.

Author Contributions: The authors confirm their contribution to the paper as follows: study conception and design, data collection, analysis and interpretation of results, and draft manuscript preparation: Jawad Raza, F. Mebarek-Oudina, Haider Ali, I. E. Sarris. All authors reviewed the results and approved the final version of the manuscript.

Availability of Data and Materials: Data are available on request.

Conflicts of Interest: The authors certify that there are no conflicts of interest about the publication of this research.

References

1. Choi, S. U., Eastman, J. A. (1995). *Enhancing thermal conductivity of fluids with nanoparticles (No. ANL/MSD/CP-84938; CONF-951135-29)*. Argonne, IL, USA: Argonne National Lab. (ANL).

2. Buongiorno, J. (2006). Convective transport in nanofluids. *Journal of Heat Transfer, 128(3),* 240–250. https://doi.org/10.1115/1.2150834

3. Sheikholeslami, M., Bhatti, M. M. (2017). Forced convection of nanofluid in presence of constant magnetic field considering shape effects of nanoparticles. *International Journal of Heat and Mass Transfer, 111(7),* 1039–1049. https://doi.org/10.1016/j.ijheatmasstransfer.2017.04.070

4. Ahmed, J., Khan, M., Ahmad, L. (2019). Stagnation point flow of Maxwell nanofluid over a permeable rotating disk with heat source/sink. *Journal of Molecular Liquids, 287(9),* 110853. https://doi.org/10.1016/j.molliq.2019.04.130

5. Imtiaz, M., Hayat, T., Alsaedi, A., Ahmad, B. (2016). Convective flow of carbon nanotubes between rotating stretchable disks with thermal radiation effects. *International Journal of Heat and Mass Transfer, 101(1),* 948–957. https://doi.org/10.1016/j.ijheatmasstransfer.2016.05.114

6. Garoosi, F., Jahanshaloo, L., Rashidi, M. M., Badakhsh, A., Ali, M. E. (2015). Numerical simulation of natural convection of the nanofluid in heat exchangers using a Buongiorno model. *Applied Mathematics and Computation, 254,* 183–203. https://doi.org/10.1016/j.amc.2014.12.116

7. Sheikholeslami, M., Ganji, D. D., Rashidi, M. M. (2016). Magnetic field effect on unsteady nanofluid flow and heat transfer using Buongiorno model. *Journal of Magnetism and Magnetic Materials, 416(45),* 164–173. https://doi.org/10.1016/j.jmmm.2016.05.026

8. Mustafa, M. (2017). MHD nanofluid flow over a rotating disk with partial slip effects: Buongiorno model. *International Journal of Heat and Mass Transfer, 108,* 1910–1916. https://doi.org/10.1016/j.ijheatmasstransfer.2017.01.064

9. Turkyilmazoglu, M. (2018). Buongiorno model in a nanofluid filled asymmetric channel fulfilling zero net particle flux at the walls. *International Journal of Heat and Mass Transfer, 126,* 974–979. https://doi.org/10.1016/j.ijheatmasstransfer.2018.05.093

10. Dharmaiah, G., Mebarek-Oudina, F., Balamurugan, K. S., Vedavathi, N. (2024). Numerical analysis of the magnetic dipole effect on a radiative ferromagnetic liquid flowing over a porous stretched sheet. *Fluid Dynamics & Materials Processing, 20*(*2*)*,* 293–310. https://doi.org/10.32604/fdmp.2023.030325

11. Sheikholeslami, M., Rokni, H. B. (2017). Effect of melting heat transfer on nanofluid flow in existence of magnetic field considering Buongiorno Model. *Chinese Journal of Physics, 55(4),* 1115–1126. https://doi.org/10.1016/j.cjph.2017.04.019

12. Tsuji, Y., Morikawa, Y., Tanaka, T., Nakatsukasa, N., Nakatani, M. (1987). Numerical simulation of gas-solid two-phase flow in a two-dimensional horizontal channel. *International Journal of Multiphase Flow, 13(5),* 671–684. https://doi.org/10.1016/0301-9322(87)90044-9

13. Hieu, P. D., Katsutoshi, T., Ca, V. T. (2004). Numerical simulation of breaking waves using a two-phase flow model. *Applied Mathematical Modelling, 28(11),* 983–1005.

14. Zeidan, D., Romenski, E., Slaouti, A., Toro, E. F. (2007). Numerical study of wave propagation in compressible two-phase flow. *International Journal for Numerical Methods in Fluids, 54(4),* 393–417.

15. Ljungqvist, M., Rasmuson, A. (2001). Numerical simulation of the two-phase flow in an axially stirred vessel. *Chemical Engineering Research and Design, 79(5),* 533–546.

16. Xue, Y., Liu, J., Liang, X., Wang, S., Ma, Z. (2022). Ecological risk assessment of soil and water loss by thermal enhanced methane recovery: Numerical study using two-phase flow simulation. *Journal of Cleaner Production, 334,* 130183.

17. Huang, Z., Yao, J., Wang, Y., Tao, K. (2011). Numerical study on two-phase flow through fractured porous media. *Science China Technological Sciences, 54,* 2412–2420.

18. Riaz, A., Tchelepi, H. A. (2006). Numerical simulation of immiscible two-phase flow in porous media. *Physics of Fluids, 18(1),* 014104.

19. Rana, P., Bhargava, R. (2012). Flow and heat transfer of a nanofluid over a nonlinearly stretching sheet: A numerical study. *Communications in Nonlinear Science and Numerical Simulation, 17(1),* 212–226.

20. Mabood, F., Khan, W. A., Ismail, A. M. (2015). MHD boundary layer flow and heat transfer of nanofluids over a nonlinear stretching sheet: A numerical study. *Journal of Magnetism and Magnetic Materials, 374,* 569–576.

21. Nadeem, S., Haq, R. U., Khan, Z. H. (2014). Numerical study of MHD boundary layer flow of a Maxwell fluid past a stretching sheet in the presence of nanoparticles. *Journal of the Taiwan Institute of Chemical Engineers, 45(1),* 121–126.

22. Pattnaik, P. K., Mishra, S. R., Barik, A. K., Mishra, A. K. (2020). Influence of chemical reaction on magnetohydrodynamic flow over an exponential stretching sheet: A numerical study. *International Journal of Fluid Mechanics Research, 47(3),* 217–228.

23. Narayana, P. S., Babu, D. H. (2016). Numerical study of MHD heat and mass transfer of a Jeffrey fluid over a stretching sheet with chemical reaction and thermal radiation. *Journal of the Taiwan Institute of Chemical Engineers, 59,* 18–25.

24. Hayat, T., Saif, R. S., Ellahi, R., Muhammad, T., Ahmad, B. (2017). Numerical study of boundary-layer flow due to a nonlinear curved stretching sheet with convective heat and mass conditions. *Results in Physics, 7,* 2601–2606.

25. Mebarek-Oudina, F., Preeti, P., Sabu, A. S., Vaidya, H., Lewis, R. W. et al. (2024). Hydromagnetic flow of magnetite-water nano-fluid utilizing adapted Buongiorno model. *International Journal of Modern Physics B, 38(1),* 2450003. https://doi.org/10.1142/S0217979224500036

26. Mahanthesh, B., Gireesha, B. J., Gorla, R. S., Makinde, O. D. (2018). Magnetohydrodynamic three-dimensional flow of nanofluids with slip and thermal radiation over a nonlinear stretching sheet: A numerical study. *Neural Computing and Applications, 30,* 1557–1567.

27. Ramesh, K., Mebarek-Oudina, F., Ismail, A. I., Jaiswal, B. R., Warke, A. S. et al. (2023). Computational analysis on radiative non-Newtonian Carreau nanofluid flow in a microchannel under the magnetic properties. *Sciencia Iranica, 30(2),* 376–390.

28. Ali, A., Mebarek-Oudina, F., Barman, A., Das, S., Ismail, A. I. (2023). Peristaltic transportation of hybrid nano-blood through a ciliated micro-vessel subject to heat source and Lorentz force. *Journal of Thermal Analysis and Calorimetry, 148(14),* 7059–7083. https://doi.org/10.1007/s10973-023-12217-x

29. Li, S., Faizan, M., Ali, F., Ramasekhar, G., Muhammad, T. et al. (2024). Modelling and analysis of heat transfer in MHD stagnation point flow of Maxwell nanofluid over a porous rotating disk. *Alexandria Engineering Journal, 91(4),* 237–248. https://doi.org/10.1016/j.aej.2024.02.002

30. Khan, N., Ali, F., Ahmad, Z., Murtaza, S., Ganie, A. H. et al. (2023). A time fractional model of a Maxwell nanofluid through a channel flow with applications in grease. *Scientific Reports, 13(1),* 4428. https://doi.org/10.1038/s41598-023-31567-y

31. Khan, M. N., Ahmad, S., Alrihieli, H. F., Wang, Z., Hussien, M. A. et al. (2023). Theoretical study on thermal efficiencies of Sutterby ternary-hybrid nanofluids with surface catalyzed reactions over a bidirectional expanding surface. *Journal of Molecular Liquids, 391(10),* 123412. https://doi.org/10.1016/j.molliq.2023.123412

32. Bejawada, S. G., Nandeppanavar, M. M. (2023). Effect of thermal radiation on magnetohydrodynamics heat transfer micropolar fluid flow over a vertical moving porous plate. *Experimental and Computational Multiphase Flow, 5(2),* 149–158. https://doi.org/10.1007/s42757-021-0131-5

33. Mebarek-Oudina, F., Chabani, I., Vaidya, H., Ismail, A. I. (2024). Hybrid nanofluid magnetoconvective flow and porous media contribution to entropy generation. *International Journal of Numerical Methods for Heat & Fluid Flow, 33(1),* 2540003. https://doi.org/10.1108/HFF-06-2023-0326

34. Mabood, F., Khan, S. U., Tlili, I. (2023). Numerical simulations for swimming of gyrotactic microorganisms with Williamson nanofluid featuring Wu's slip, activation energy and variable thermal conductivity. *Applied Nanoscience, 13(5),* 131–144. https://doi.org/10.1007/s13204-020-01548-y

35. Ijaz Khan, M., Alzahrani, F. (2020). Activation energy and binary chemical reaction effect in nonlinear thermal radiative stagnation point flow of Walter-B nanofluid: Numerical computations. *International Journal of Modern Physics B, 34(13),* 2050132. https://doi.org/10.1142/S0217979220501325

36. Ramesh, K., Mebarek-Oudina, F., Souayeh, B. (2023). *Mathematical modelling of fluid dynamics and nanofluids,* 1st edition. CRC Press (Taylor & Francis). https://doi.org/10.1201/9781003299608